Check for updates

# Simple fabrication of $Co_3O_4$ nanoparticles on N-doped laser-induced graphene for high-performance supercapacitors†

Mahima Khandelwal,*[a] Anh Phan Nguyen,[ab] Chau Van Tran[a] and Jung Bin In [iD] *[ab]

This study demonstrates a simple strategy to fabricate $Co_3O_4$ on N-doped laser-induced graphene ($Co_3O_4$-NLIG) based on duplicate laser pyrolysis, enabling the *in situ* generation of $Co_3O_4$ nanoparticles and heteroatom doping in laser-induced graphene (LIG). Morphological analyses reveal the uniform distribution of $Co_3O_4$ nanoparticles on the surface of the LIG structure. The modification of NLIG with $Co_3O_4$ nanoparticles results in impressive electrochemical performance due to the contributions from electric double-layer capacitance and pseudocapacitance. The optimal $Co_3O_4$-NLIG is produced at 20 wt% cobalt precursor loading ($Co_3O_4$-NLIG-20). In a three-electrode setup, this electrode exhibits a specific areal capacitance ($C_A$) of 216.3 mF cm$^{-2}$ at a current density of 0.5 mA cm$^{-2}$ in a 1 M KOH electrolyte. When the optimal electrodes are assembled into a solid-state supercapacitor ($Co_3O_4$-NLIG-SC) using a poly(vinyl alcohol) phosphoric acid (PVA–$H_3PO_4$) gel electrolyte, a $C_A$ of 17.96 mF cm$^{-2}$ is obtained with good cycling stability.

## 1. Introduction

The efficient use of renewable energy resources requires the development of high-performance energy storage devices. As a promising energy storage device, the potential of super-capacitors (SCs) has been explored due to their rapid charge–discharge capability, long-term cyclability, high power capability, and safe operation.[1,2] Electrodes of SCs play a critical role in determining the performance for energy storage. Thus, the development of high-performance electrodes has been actively pursued. Graphene or graphene-based materials have been commonly used as high-performance electrode materials for SCs due to their favorable physiochemical properties.[3] However, conventional synthesis methods for graphene-based materials are highly complex and costly to implement, usually requiring long reaction times, undesirable harsh experimental conditions, and post-synthesis treatment. Therefore, a recent goal is to develop an efficient, simple method for directly synthesizing graphene-based materials applicable for SCs.

Recently, graphene fabrication *via* laser-induced pyrolysis of polymers has attracted significant attention from the research community due to its cost-effective and facile fabrication

processing.[4,5] As-obtained laser-induced graphene (LIG), which is immediately obtained by irradiating a polymer with a laser beam, features porous structure with high thermal and electrical conductivity. It has been used for various applications: electrochemical sensing,[6] environmental,[7] microfluidic devices,[8] nanogenerators,[9,10] electrocatalysis,[11,12] and SCs.[4,13,14] Among them, LIG is commonly used as an electrode material for SCs. However, the capacitance and energy density of pure LIG is relatively low, possibly due to the limited surface of electrode material accessible to electrolyte ions.[15]

Therefore, efforts have been made to modify the LIG surface by heteroatom doping (N, S, B, and P),[16–18] functionalization,[19] and producing hybrid composites with pseudocapacitive materials.[20–22] For instance, heteroatom-doped LIG electrode material exhibited significantly improved capacitive performance compared with pristine LIG, as previously reported by our research group.[18] The integration of heteroatom-doped LIG with pseudocapacitive material is also a viable strategy to boost the electrochemical performance of SC electrode materials. Of the pseudocapacitive materials, $Co_3O_4$ is promising due to its cost-effectiveness, environmental friendliness, and high theoretical capacitance. Thus, the development of a hybrid LIG electrode that incorporates heteroatom and pseudocapacitive components based on a simple, cost-effective, and energy-efficient method is highly promising for improving electrochemical performance of LIG.

In this study, we demonstrate the *in situ* fabrication of $Co_3O_4$-decorated N-doped LIG ($Co_3O_4$-NLIG) using the duplicate laser-induction method, which involves two laser irradiation processes. The effect of varying the wt% of $Co^{2+}$ precursor is

*[a] Soft Energy Systems and Laser Applications Laboratory, School of Mechanical Engineering, Chung-Ang University, Seoul 06974, Republic of Korea. E-mail: mahimaiitr@gmail.com; jbin@cau.ac.kr*

*[b] Department of Intelligent Energy and Industry, Chung-Ang University, Seoul 06974, Republic of Korea*

significant for modifying the surface of NLIG with $Co_3O_4$ and thus its electrochemical performance. The optimal $Co_3O_4$-NLIG with 20 wt% cobalt precursor loading ($Co_3O_4$-NLIG-20) has a specific areal capacitance ($C_A$) of 216.3 mF cm$^{-2}$ at a current density of 0.5 mA cm$^{-2}$ using a three-electrode setup in a 1 M KOH electrolyte, which is considerably higher than that of NLIG (1.4 mF cm$^{-2}$). Moreover, when assembled into a solid-state SC ($Co_3O_4$-NLIG-SC), the hybrid electrode exhibits a $C_A$ value of 17.96 mF cm$^{-2}$ at a current density of 0.1 mA cm$^{-2}$ with high cycling stability (>70% capacitance retention after 5000 charge–discharge cycles).

## 2. Experimental section

### 2.1. Materials

Materials included a polyimide (PI) sheet (Kapton HN, thickness: 125 μm, McMaster-Carr), polyamic acid (PAA; 80% $N$-methyl-2-pyrrolidone/20% aromatic hydrocarbon, Sigma-Aldrich), cobalt chloride hexahydrate ($CoCl_2 \cdot 6H_2O$, Sigma-Aldrich), poly(vinyl alcohol) (PVA; $M_w$: 89 000–98 000, >99% hydrolyzed, Sigma-Aldrich), potassium hydroxide pellets (KOH; Sigma-Aldrich), phosphoric acid solution ($H_3PO_4$; 85 wt%, Sigma-Aldrich), and deionized water (DIW; Sigma-Aldrich).

### 2.2. Synthesis of $Co_3O_4$-decorated N-doped laser-induced graphene ($Co_3O_4$-NLIG)

The synthesis of $Co_3O_4$-NLIG was conducted using the two-step laser pyrolysis method. In the first step, LIG (s-LIG) was obtained by irradiating the commercial PI sheet using a carbon dioxide ($CO_2$) laser (v30+, 10.6 μm wavelength, Synrad), as reported previously.[23] The PAA solution was mixed with different concentrations of $CoCl_2 \cdot 6H_2O$ (5, 10, and 20 wt%) at room temperature (~25 °C). Next, the homogenous mixture of PAA and $CoCl_2 \cdot 6H_2O$ was drop-casted on s-LIG followed by spin-coating.[23]

The PAA- and $CoCl_2 \cdot 6H_2O$-coated s-LIG film was then placed on a hot plate at 250 °C for 30 min to conduct the imidization of PAA to PI followed by the second laser pyrolysis to obtain $Co_3O_4$-NLIG. The laser power, scanning speed, frequency, and raster-scanning pitch were set at 3.5 W, 200 mm s$^{-1}$, 20 kHz, and 0.125 mm, respectively, for the second laser pyrolysis. The $Co_3O_4$-NLIG obtained at different concentrations of $CoCl_2 \cdot 6H_2O$ was denoted as $Co_3O_4$-NLIG-$x$, where $x$ represents 5, 10, and 20 wt% $CoCl_2 \cdot 6H_2O$ in PAA. Similarly, N-doped LIG (NLIG) was produced by following the above procedure without adding $CoCl_2 \cdot 6H_2O$ to the PAA solution.

### 2.3. Material characterization

Raman spectra were recorded on a micro-Raman spectrometer (FEX, NOST) using a 532 nm laser in the wavenumber range of 2000–100 cm$^{-1}$. Surface morphologies were captured on a field-emission scanning electron microscope (FESEM; Carl Zeiss, SIGMA 300). Transmission electron microscopy (TEM), high-resolution TEM (HRTEM), and selected area diffraction (SAED) patterns were recorded on a JEOL JEM-2100F at an accelerating voltage of 200 keV. X-ray photoelectron spectroscopy (XPS) measurements were recorded on a Thermo Fisher Scientific K-alpha+ spectrometer. TEM samples were prepared by dispersing a small amount of LIG powder in chloroform using sonication. The Cu grid was subsequently immersed in the dispersion solution and dried under ambient conditions.

### 2.4. Electrochemical measurements

Electrochemical measurements were performed in the three-electrode system using saturated calomel electrode (SCE), Pt wire, and $Co_3O_4$-NLIG as the reference, counter, and working electrodes, respectively. The active area of the working electrodes was maintained at 1 cm$^2$. Cyclic voltammetry (CV) and galvanostatic charge–discharge (GCD), and electrochemical impedance spectroscopy (EIS) measurements were performed on an SP-150, Bio-Logic electrochemical workstation using 1 M KOH aqueous electrolyte in the potential window of −0.2–0.5 V. EIS measurements were recorded in the frequency range varying from 0.01 Hz to 100 kHz at a sinusoidal amplitude of 10 mV.

### 2.5. Fabrication of solid-state SC

Two identically sized (1 × 1 cm$^2$) working electrodes were used to fabricate a solid-state SC. At the end of each working electrode, copper strips (functioning as current collectors) were attached. The contact resistance between the working electrode and current collector was minimized by applying a conductive silver paste at the electrode interface. Next, the current collector was covered with insulating PI Kapton tape to prevent its contact with the gel electrolyte. Subsequently, the working electrodes were uniformly coated with ~50 μL of PVA–$H_3PO_4$ gel electrolyte and dried under ambient conditions (~24 h) to evaporate excess water. Finally, the electrodes were constructed into a sandwich-type solid-state SC.

The PVA–$H_3PO_4$ gel electrolyte was fabricated by dissolving 3 g of PVA in 30 mL of DIW by stirring at 95 °C for ~6 h. Next, 2 mL of $H_3PO_4$ solution was added gradually to the transparent PVA solution and then stirred for another 3–4 h to obtain the gel electrolyte.

## 3. Results and discussion

### 3.1. Fabrication and characterization of $Co_3O_4$-NLIG

Fig. 1 is a schematic of the preparation of $Co_3O_4$-NLIG based on the double pyrolysis method developed by our research group.[23] In the first step, s-LIG (1 × 1.5 cm$^2$) was prepared from the commercial PI sheet which contains negligible N content (0.3 at%) as has been observed previously.[23] Next, the PAA solution mixed with different concentrations of $CoCl_2 \cdot 6H_2O$ (5, 10, and 20 wt%) was drop-casted on the s-LIG film and kept for 10 min under ambient conditions. The inherently porous structure of s-LIG enabled the uniform adsorption of the PAA/$Co^{2+}$ precursor solution. Next, the PAA/$Co^{2+}$ precursor-coated s-LIG film was spin-coated and subsequently imidized to induce the conversion of PAA to PI, and duplicate pyrolysis was conducted to obtain $Co_3O_4$-NLIG. Duplicate laser irradiation triggered the

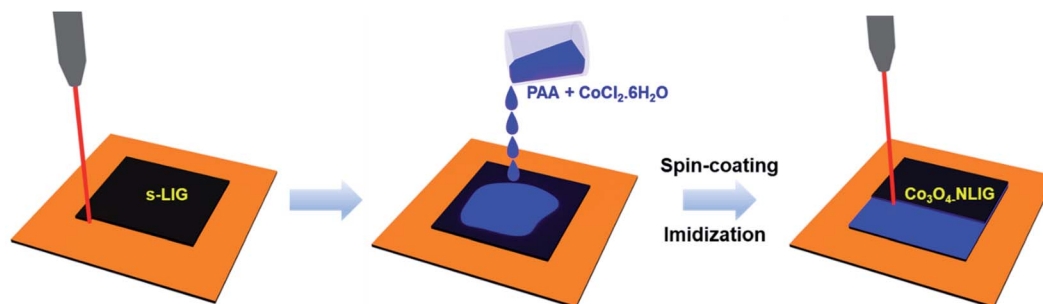Fig. 1 Schematic of $Co_3O_4$-NLIG synthesis.

simultaneous formation of $Co_3O_4$ and heteroatom doping in LIG.

Fig. 2a presents the Raman spectra of NLIG and $Co_3O_4$-NLIG-20. Both samples exhibit two distinctive peaks corresponding to D and G bands. The D band appears due to the presence of structural disorders and defects, and the G band is assigned to $sp^2$ graphitic domains in the carbon framework.[18] The intensity ratio of D and G bands ($I_D/I_G$) is used to identify the level of disorders and defects in the graphitic structure. The $I_D/I_G$ ratio of $Co_3O_4$-NLIG-20 (1.34) is higher than that of NLIG (0.87), suggesting that the presence of $Co_3O_4$ on NLIG increases defects and disorders. Besides the presence of the two distinctive D and G bands, $Co_3O_4$-NLIG-20 has a distinct, characteristic peak at approximately 198 $cm^{-1}$, corresponding to the $F_{2g}^1$ mode of $Co_3O_4$.[24,25]

Furthermore, XPS measurements were conducted to determine the elemental compositions and surface chemical states

of $Co_3O_4$-NLIG-20 and NLIG. The survey scan spectra of NLIG and $Co_3O_4$-NLIG-20 in the binding energy range of 0–1300 eV exhibit peaks corresponding to C1s, N1s, and O1s elements with the presence of an additional Co 2p peak in the latter sample (Fig. 2b). Table S1† summarizes the elemental compositions (at%) of C, O, N, and Co. High-resolution C1s and N1s spectra of NLIG are illustrated in Fig. S1.† The high-resolution C1s and N1s in $Co_3O_4$-NLIG-20 exhibit peaks at binding energies of 284.8 and 401.0 eV, respectively (Fig. 2c and d). Further, the high resolution C1s spectrum is deconvoluted into four peaks corresponding to C–C ($sp^2/sp^3$) (284.8 eV), C–N (285.3 eV), C–O (286.5 eV), and $\pi$–$\pi$* (291.1 eV).[23] On the other hand, the high resolution N1s spectrum is deconvoluted into three characteristic peaks corresponding to pyridinic-N (399.3 eV), pyrrolic-N (400.7 eV), and quaternary-N (401.5 eV).[23]

The high-resolution Co 2p spectrum has two characteristic peaks of $Co_3O_4$ at 778.5 and 793.5 eV corresponding to Co $2p_{3/2}$
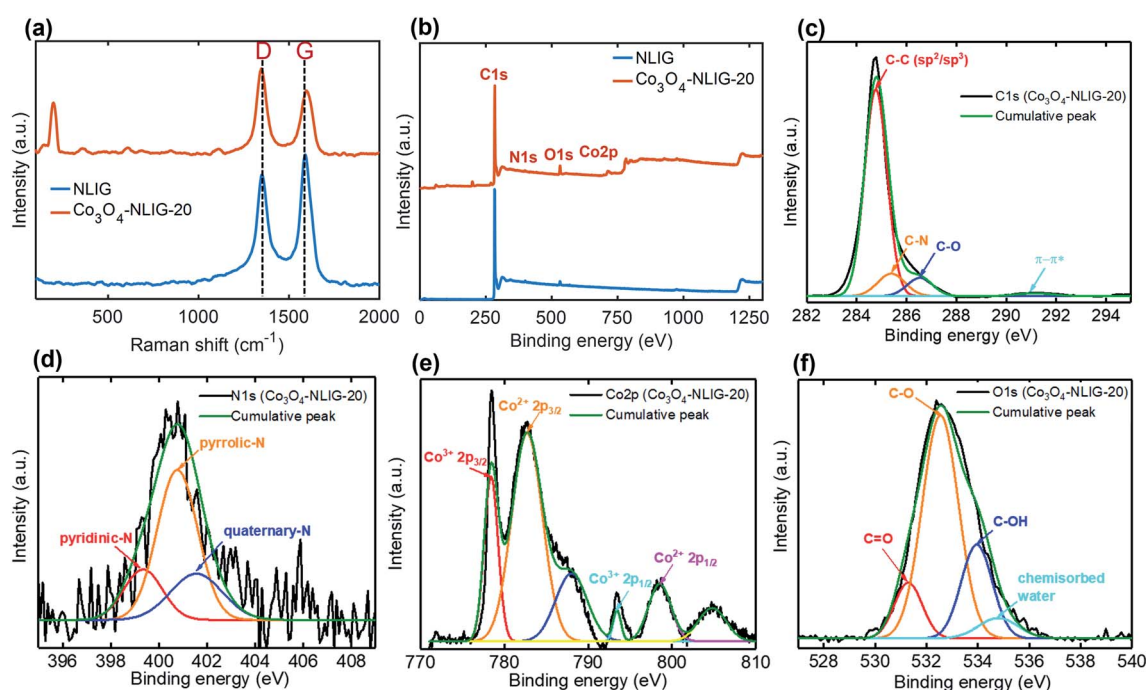


Fig. 2 (a) Raman spectra of NLIG and $Co_3O_4$-NLIG-20. (b) XPS survey scan spectra of NLIG and $Co_3O_4$-NLIG-20. (c) High-resolution C1s, (d) N1s, (e) Co2p, and (f) O1s spectra of $Co_3O_4$-NLIG-20.
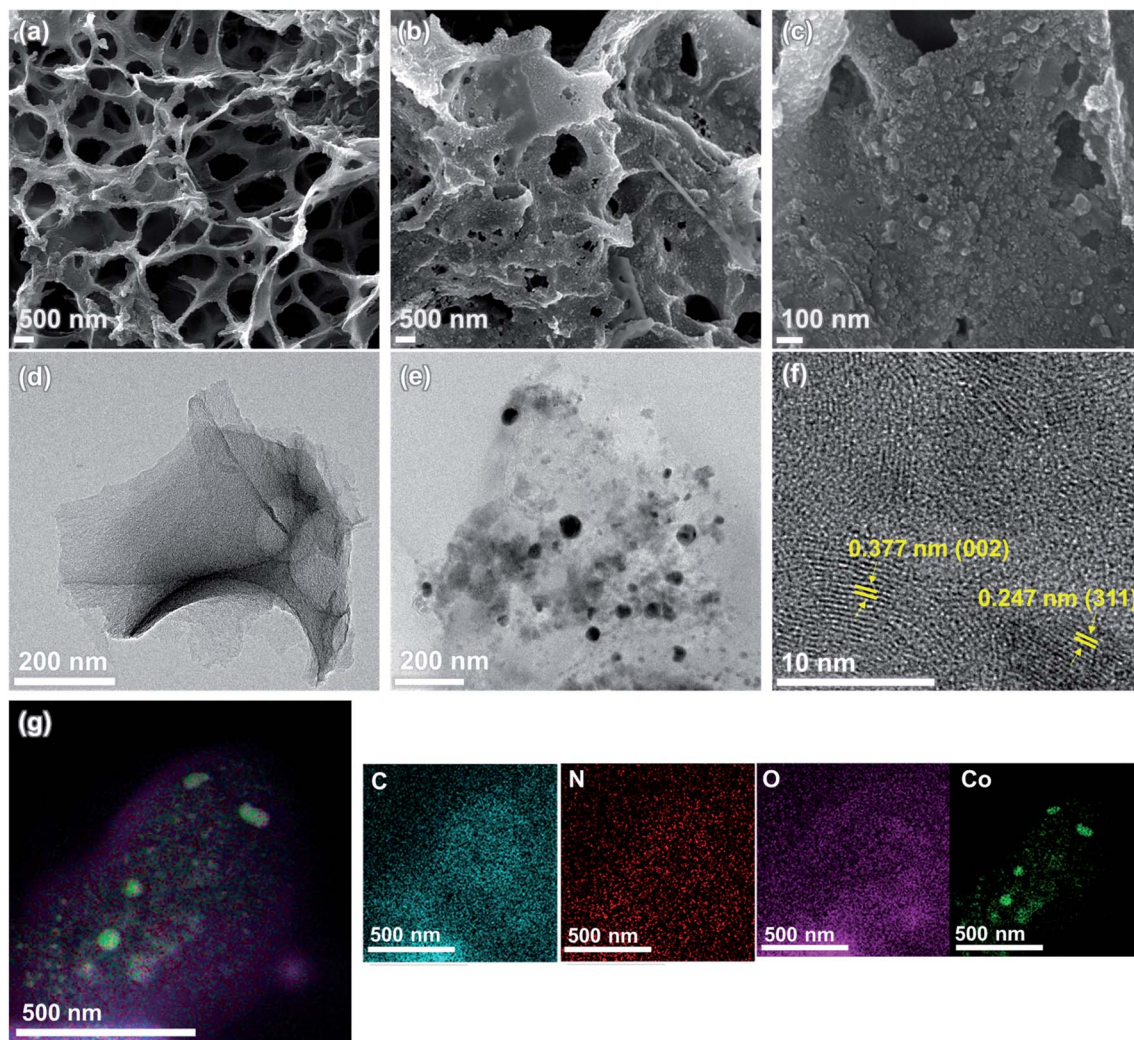
**Fig. 3** FESEM images of (a) NLIG and (b) $Co_3O_4$-NLIG-20. (c) High-magnification FESEM image of $Co_3O_4$-NLIG-20. TEM images of (d) NLIG and (e) $Co_3O_4$-NLIG-20. HRTEM image of (f) $Co_3O_4$-NLIG-20. TEM image of (g) $Co_3O_4$-NLIG-20 of overlapped C, N, O, and Co.

and Co $2p_{1/2}$, respectively, with spin–orbit splitting of 15 eV.[24] The presence of the other two satellite peaks at binding energies of 788.1 and 805.3 eV agrees closely with previous studies.[24] Moreover, the peaks at 782.7 and 798.6 eV have been assigned to $Co^{2+}$, similar to previous studies.[26] The O1s spectrum shows four peaks at 531.2, 532.5, 533.9, and 534.8 eV corresponding to C=O, C–O, C–OH, and chemisorbed water, respectively.[27,28] The XPS results suggest the formation of $Co_3O_4$ and doping of N.

The structural and morphological features of NLIG and $Co_3O_4$-NLIG-20 samples were examined using FE-SEM and TEM, as illustrated in Fig. 3. NLIG exhibits a typical interconnected porous structure caused by the rapid release of gases during laser scanning. In contrast, $Co_3O_4$-NLIG-20 exhibits a uniform decoration of spherical particles, indicating the successful synthesis of $Co_3O_4$ on the surface of NLIG. Furthermore, the cross-sectional images have been recorded for NLIG and $Co_3O_4$-NLIG-20 and shown in Fig. S2.† From the cross-sectional images, the average thicknesses of NLIG and $Co_3O_4$-NLIG-20 were estimated to be 52.6 and 59.4 μm, respectively.

Moreover, the electrical conductivity of $Co_3O_4$-NLIG-20 film is measured to be 10.63 S $cm^{-1}$.

Furthermore, the TEM image depicts the uniform decoration of $Co_3O_4$ nanoparticles on the sheet-like LIG structure. The size of the $Co_3O_4$ nanoparticles is estimated to be in the range of 19–40 nm. Furthermore, the HRTEM image of $Co_3O_4$-NLIG illustrates distinct lattice fringes, demonstrating the crystalline nature of $Co_3O_4$ nanoparticles on LIG. Based on these lattice fringes, the d-spacing is calculated to be 0.247 nm, assigned to the (311) plane of $Co_3O_4$, agreeing closely with previous studies.[20] The image also illustrates the lattice fringe with d-spacing of 0.377 nm, corresponding to the graphitic structure of LIG. Furthermore, the SAED pattern of $Co_3O_4$-NLIG reveals concentric rings with diffraction spots, suggesting the polycrystalline nature of $Co_3O_4$-NLIG, unlike NLIG (Fig. S3†). The elemental mapping images of $Co_3O_4$-NLIG-20 (Fig. 3g) illustrate the presence of carbon (C), nitrogen (N), oxygen (O), and cobalt (Co).
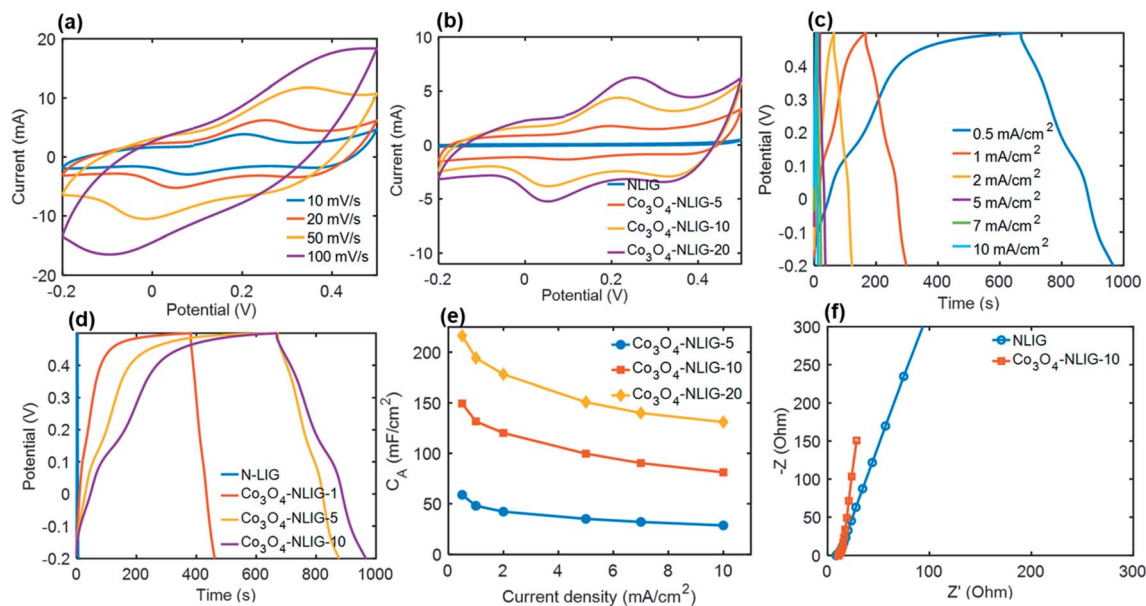
Fig. 4 (a) CV curves of $Co_3O_4$-NLIG-20 at different scan rates varying from 10 to 100 mV s$^{-1}$. (b) Comparative CV curves of $Co_3O_4$-NLIG-$x$ electrodes prepared by varying wt% $Co^{2+}$ precursor with NLIG. (c) GCD curves of $Co_3O_4$-NLIG-20 at different current densities varying from 0.5 to 10 mA cm$^{-2}$. (d) Comparative GCD curves of $Co_3O_4$-NLIG-$x$ electrodes prepared by varying wt% $Co^{2+}$ precursor with NLIG. (e) $C_A$ of different $Co_3O_4$-NLIG-$x$ samples with current density. (f) EIS curves of $Co_3O_4$-NLIG-20 and NLIG.

## 3.2. Electrochemical measurements

The electrochemical performance of different $Co_3O_4$-NLIG-$x$ prepared by varying the wt% of the $Co^{2+}$ precursor was characterized by CV and GCD measurements (Fig. 4). All

electrochemical measurements were performed in the potential window of −0.2–0.5 V vs. SCE in a 1 M KOH electrolyte using a three-electrode system. Fig. 4a illustrates the CV curve of the optimal $Co_3O_4$-NLIG-20 electrode material at different scan



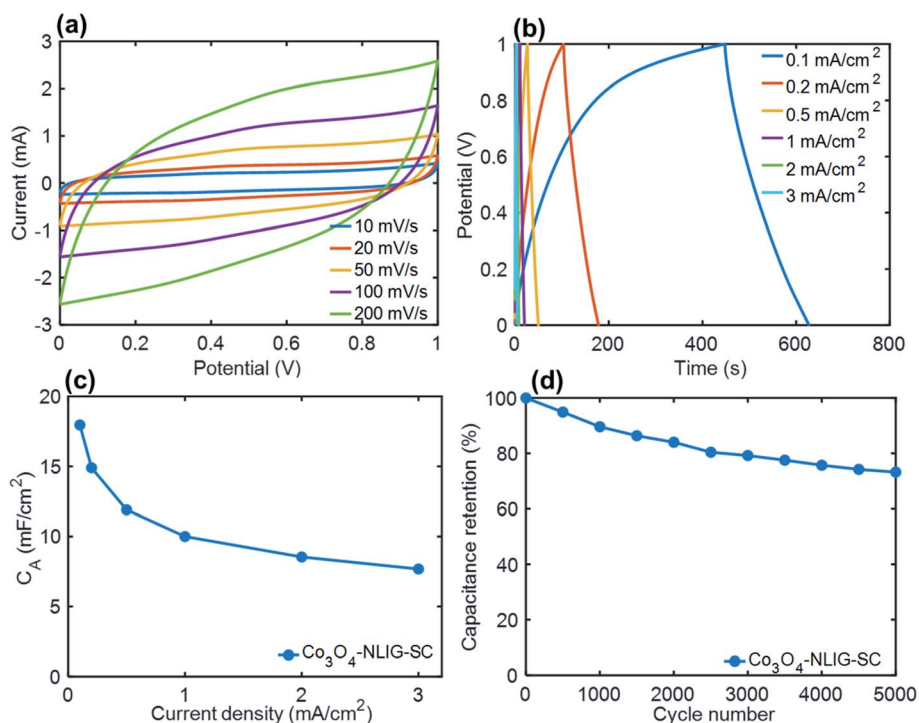Fig. 5 (a) CV curves of $Co_3O_4$-NLIG-SC at different scan rates. (b) GCD curves of $Co_3O_4$-NLIG-SC at different current densities. (c) Variation in $C_A$ with current density. (d) Cycling stability test of $Co_3O_4$-NLIG-SC at current density of 2 mA cm$^{-2}$.

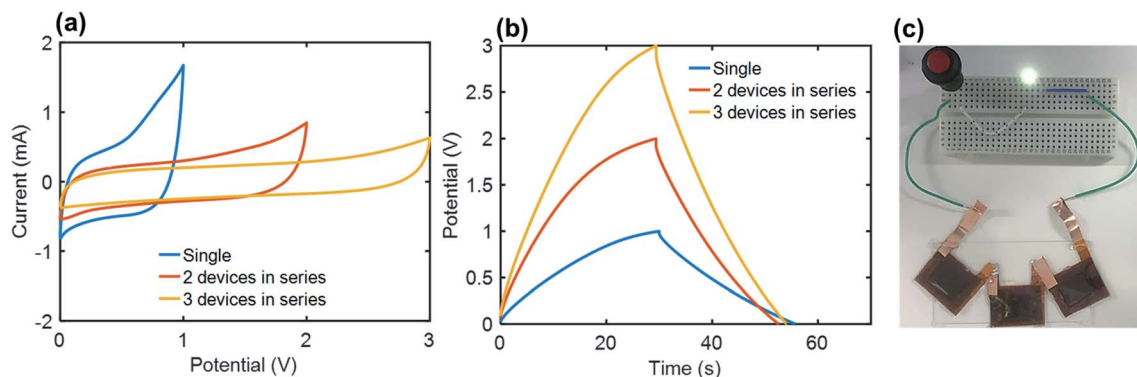**Fig. 6** (a) CV curves at 50 mV s$^{-1}$ (b) and GCD curves at 0.5 mA cm$^{-2}$ of one, two, and three Co$_3$O$_4$-NLIG-SCs connected in series. (c) Digital image of a green LED powered by three Co$_3$O$_4$-NLIG-SCs devices connected in series.

rates varying from 10 to 100 mV s$^{-1}$, revealing the distorted shape of CV curves caused by the pseudocapacitive contribution from Co$_3$O$_4$, similar to previous studies.[24,29] Fig. 4b illustrates the comparison of different Co$_3$O$_4$/NLIG-$x$ electrode materials with NLIG at a scan rate of 20 mV s$^{-1}$. Unlike NLIG, the CV curve of the Co$_3$O$_4$-NLIG-$x$ electrode material exhibits two distinctive oxidation peaks corresponding to the conversion between two different oxidation states of cobalt (Co$^{2+}$/Co$^{3+}$), as follows:[24,29,30]

$$Co_3O_4 + OH^- + H_2O \Leftrightarrow 3CoOOH + e^-$$

$$CoOOH + OH^- \Leftrightarrow CoO_2 + H_2O + e^-$$
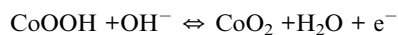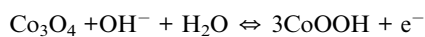
Based on the comparative CV curves recorded at a scan rate of 20 mV s$^{-1}$, the area covered under the CV curve for Co$_3$O$_4$-NLIG-$x$ electrode materials is much larger than for NLIG. A gradual increase in current was observed as the loading of the Co precursor increased from 5 to 20 wt%. The further increase in the concentration of the Co$^{2+}$ precursor in the PAA solution resulted in gelation of the solution, which caused the non-uniform deposition of Co$_3$O$_4$ on NLIG and decreased $C_A$. Therefore, the Co$_3$O$_4$-NLIG electrode with the 20 wt% Co$^{2+}$ precursor had the best capacitive properties. The maximum areal specific capacitance ($C_A$) was calculated for Co$_3$O$_4$-NLIG-20 (155 mF cm$^{-2}$) when compared with Co$_3$O$_4$-NLG-10 (119.3 mF cm$^{-2}$), Co$_3$O$_4$-NLG-5 (54.6 mF cm$^{-2}$), and NLIG (3.57 mF cm$^{-2}$). The significantly enhanced capacitance of the Co$_3$O$_4$-NLIG-$x$ electrode material compared with NLIG was ascribed to the synergistic effect between Co$_3$O$_4$ and NLIG.

The capacitive performance of electrode materials was investigated by conducting GCD measurements. Fig. 4c presents the GCD curves of the Co$_3$O$_4$-NLIG-20 electrode material at various current densities. At all current densities, the discharge curve illustrates pseudocapacitive characteristics. A comparative GCD curve at a current density of 0.5 mA cm$^{-2}$ illustrates a much higher $C_A$ value for Co$_3$O$_4$-NLIG-20 (216.3 mF cm$^{-2}$) when compared with Co$_3$O$_4$-NLIG-10 (149.4 mF cm$^{-2}$) and Co$_3$O$_4$-NLIG-5 (58.9 mF cm$^{-2}$) (Fig. 4d), similar to the CV results.

Furthermore, the $C_A$ for Co$_3$O$_4$-NLIG-20 (216.3 mF cm$^{-2}$) increased dramatically compared with that for NLIG (1.4 mF

cm$^{-2}$) at the same current density due to the pseudocapacitive behavior of Co$_3$O$_4$. Fig. 4e illustrates the variation in $C_A$ with the change in current density from 0.5 to 10 mA cm$^{-2}$. As illustrated in Fig. 4e, the increase in the current density decreases $C_A$ due to the increased potential drop and lack of pseudocapacitance contribution at high current densities.

Fig. 4f illustrates the Nyquist plot of the NLIG and Co$_3$O$_4$-NLIG-20 electrode materials. Both samples exhibit high- and low-frequency regions related to the charge-transfer resistance at the electrode–electrolyte interface and diffusion of ions, respectively. The Co$_3$O$_4$-NLIG-20 sample has more vertical lines than NLIG, suggesting ideal capacitive behavior.

### 3.3. Electrochemical performance of all-solid-state SC

A solid-state SC was constructed with two identical (1 × 1 cm$^2$) Co$_3$O$_4$-NLIG-20 electrodes and a PVA–H$_3$PO$_4$ gel electrolyte—denoted as Co$_3$O$_4$-NLIG-SC. Fig. 5a illustrates the quasi-rectangular CV curve shape at different scan rates, suggesting the significant contribution of pseudocapacitance due to the presence of Co$_3$O$_4$ on LIG. Similarly, GCD curves were recorded at different current densities varying from 0.1 to 3 mA cm$^{-2}$ (Fig. 5b).

The GCD curve of Co$_3$O$_4$-NLIG-SC exhibited a distorted triangular curve shape, with a $C_A$ of 17.96 mF cm$^{-2}$ at a current density of 0.1 mA cm$^{-2}$. The $C_A$ value for Co$_3$O$_4$-NLIG-SC is higher than or comparable with those of the heteroatom-doped LIG and LIG composite with metal oxides (Table S2†). Multiple cycles at each current density is shown in Fig. S4.† Furthermore, a long cycling stability test was performed for Co$_3$O$_4$-NLIG-SC at a current density of 2 mA cm$^{-2}$, which exhibited a capacitance retention above 70%. The EIS curve of Co$_3$O$_4$-NLIG-SC shows nearly vertical line at low frequency region suggesting its capacitive behavior. The equivalent series resistance (ESR) measured from $x$-intercept of Nyquist plot is found to be 18 Ω (Fig. S5†). Furthermore, the flexibility test was performed for Co$_3$O$_4$-NLIG-SC under different bending radii (5 to 25 mm) at a current density of 1 mA cm$^{-2}$ (Fig. S6†). The capacitance retention is found to be >98% under different bending radii suggesting the excellent flexibility of Co$_3$O$_4$-NLIG-SC.

Moreover, $Co_3O_4$-NLIG-SC exhibited a relatively high energy density of 2.49 $\mu$W h cm$^{-2}$ at a power density of 0.05 mW cm$^{-2}$. It may be mentioned that the energy density of $Co_3O_4$-NLIG-SC (2.49 $\mu$W h cm$^{-2}$) is found to be higher than previously reported SCs/micro-supercapacitor (MSC) at similar power density such as LIG MSC (0.9 $\mu$W h cm$^{-2}$),[14] NiO/$Co_3O_4$/LIG-WPU (0.124 $\mu$W h cm$^{-2}$),[31] B-LIG MSC (2.29 $\mu$W h cm$^{-2}$),[16] $MnO_2$-rGO//$MnO_2$-CNT MSC (0.66 $\mu$W h cm$^{-2}$),[32] 3D graphene MSC (0.38 $\mu$W h cm$^{-2}$) at similar power density.[33] However, the energy density obtained in the present work is smaller than the previously reported LIG/$MoO_2$ core–shell electrode on carbon cloth.[34]

In order to meet the practical requirements for the voltage and specific energy, three $Co_3O_4$-NLIG-SCs were connected in series and their CV and GCD measurements were recorded at 50 mV s$^{-1}$ and 0.5 mA cm$^{-2}$, respectively (Fig. 6a and b). The linear increase in the operating voltage is consistent for a single (1 V), two (2 V), and three (3 V) $Co_3O_4$-NLIG-SCs devices connected in series. Thereafter, three $Co_3O_4$-NLIG-SCs devices were assembled in series which can successfully illuminate a green light-emitting diode (LED), demonstrating the potential of $Co_3O_4$-NLIG-SC for practical application (Fig. 6c).

# 4. Conclusions

This study successfully demonstrated the fabrication of $Co_3O_4$ on N-doped LIG based on duplicate laser pyrolysis. Duplicate laser pyrolysis enabled the simultaneous formation of $Co_3O_4$ and heteroatom doping in LIG. Due to the beneficially synergistic effects of NLIG and $Co_3O_4$, the optimal $Co_3O_4$-NLIG-20 electrode material exhibited impressive electrochemical performance with a $C_A$ value of 216.3 mF cm$^{-2}$ at a current density of 0.5 mA cm$^{-2}$ in a three-electrode system. Furthermore, when assembled into a solid-state SC, $Co_3O_4$-NLIG-SC demonstrated electrochemical performance comparable to previously reported data on LIG with metal oxide composites. Consequently, this strategy is viable for fabricating LIG decorated with metal oxide, which can be used for SC applications.

# Conflicts of interest

There are no conflicts to declare.

# Acknowledgements

# References

1 J. R. Miller and P. Simon, *Science*, 2008, **321**, 651.

2 J. R. Miller and A. Burke, *Electrochem. Soc. Interface*, 2008, **17**, 53–57.

3 L. L. Zhang, R. Zhou and X. S. Zhao, *J. Mater. Chem.*, 2010, **20**, 5983–5992.

4 R. Ye, D. K. James and J. M. Tour, *Adv. Mater.*, 2019, **31**, e1803621.

5 J. B. In, B. Hsia, J. H. Yoo, S. Hyun, C. Carraro, R. Maboudian and C. P. Grigoropoulos, *Carbon*, 2015, **83**, 144–151.

6 A. A. Lahcen, S. Rauf, T. Beduk, C. Durmus, A. Aljedaibi, S. Timur, H. N. Alshareef, A. Amine, O. S. Wolfbeis and K. N. Salama, *Biosens. Bioelectron.*, 2020, **168**, 112565.

7 L. Cheng, W. Guo, X. Cao, Y. Dou, L. Huang, Y. Song, J. Su, Z. Zeng and R. Ye, *Mater. Chem. Front.*, 2021, **5**, 4874–4891.

8 K. W. Tan, B. Jung, J. G. Werner, E. R. Rhoades, M. O. Thompson and U. Wiesner, *Science*, 2015, **349**, 54.

9 M. G. Stanford, J. T. Li, Y. Chyan, Z. Wang, W. Wang and J. M. Tour, *ACS Nano*, 2019, **13**, 7166–7174.

10 P. Zhao, G. Bhattacharya, S. J. Fishlock, J. G. M. Guy, A. Kumar, C. Tsonos, S. Yu, S. Raj, J. A. McLaughlin, J. Luo and N. Soin, *Nano Energy*, 2020, **75**, 104958.

11 M. Ren, J. Zhang and J. M. Tour, *Carbon*, 2018, **139**, 880–887.

12 M. Ren, J. Zhang, C. Zhang, M. G. Stanford, Y. Chyan, Y. Yao and J. M. Tour, *ACS Appl. Energy Mater.*, 2020, **3**, 1702–1709.

13 X. Li, W. Cai, K. S. Teh, M. Qi, X. Zang, X. Ding, Y. Cui, Y. Xie, Y. Wu, H. Ma, Z. Zhou, Q.-A. Huang, J. Ye and L. Lin, *ACS Appl. Mater. Interfaces*, 2018, **10**, 26357–26364.

14 Z. Peng, J. Lin, R. Ye, E. L. G. Samuel and J. M. Tour, *ACS Appl. Mater. Interfaces*, 2015, 7, 3414–3419.

15 K. Y. Kim, H. Choi, C. Van Tran and J. B. In, *J. Power Sources*, 2019, **441**, 227199.

16 Z. Peng, R. Ye, J. A. Mann, D. Zakhidov, Y. Li, P. R. Smalley, J. Lin and J. M. Tour, *ACS Nano*, 2015, **9**, 5868–5875.

17 Y. Rao, M. Yuan, F. Luo, Z. Wang, H. Li, J. Yu and X. Chen, *Carbon*, 2021, **180**, 56–66.

18 M. Khandelwal, C. V. Tran, J. Lee and J. B. In, *Chem. Eng. J.*, 2022, **428**, 131119.

19 R. Shi, J. Long, X. Zou, G. Fu, L. Yu, Y. Tian, Y. Chen and F. Luo, *Catal. Lett.*, 2021, DOI: 10.1007/s10562-021-03786-3.

20 R. Xu, P. Liu, G. Ji, L. Gao and J. Zhao, *ACS Appl. Energy Mater.*, 2020, **3**, 10676–10684.

21 W. Wang, L. Lu, Y. Xie, X. Mei, Y. Tang, W. Wu and R. Liang, *Appl. Surf. Sci.*, 2020, **504**, 144487.

22 R. Xu, Z. Wang, L. Gao, S. Wang and J. Zhao, *Appl. Surf. Sci.*, 2022, **571**, 151385.

23 M. Khandelwal, C. V. Tran and J. B. In, *Appl. Surf. Sci.*, 2022, **576**, 151714.

24 Y. Li, D. Pan, M. Zhang, J. Xie and Z. Yan, *RSC Adv.*, 2016, **6**, 48357–48364.

25 M. Khandelwal, S. Chandrasekaran, S. H. Hur and J. S. Chung, *J. Power Sources*, 2018, **407**, 70–83.

26 I. Rabani, J. Yoo, H.-S. Kim, D. V. Lam, S. Hussain, K. Karuppasamy and Y.-S. Seo, *Nanoscale*, 2021, **13**, 355–370.

27 A. Ganguly, S. Sharma, P. Papakonstantinou and J. Hamilton, *J. Phys. Chem. C*, 2011, **115**, 17009–17019.

28 J. V. Rojas, M. Toro-Gonzalez, M. C. Molina-Higgins and C. E. Castano, *Mater. Sci. Eng., B*, 2016, **205**, 28–35.

29 Q. Li, X. Hu, Q. Yang, Z. Yan, L. Kang, Z. Lei, Z. Yang and Z. Liu, *Electrochim. Acta*, 2014, **119**, 184–191.

30 K. J. Samdani, S. H. Kim, J. H. Park, S. H. Hong and K. T. Lee, *J. Ind. Eng. Chem.*, 2019, **74**, 96–102.

31 W. Wang, L. Lu, Y. Xie, W. Yuan, Z. Wan, Y. Tang and K. S. Teh, *Adv. Mater. Technol.*, 2020, **5**, 1900903.

32 B. D. Boruah, A. Maji and A. Misra, *ACS Appl. Mater. Interfaces*, 2018, **10**, 15864–15872.

33 L. Zhang, D. DeArmond, N. T. Alvarez, R. Malik, N. Oslin, C. McConnell, P. K. Adusei, Y.-Y. Hsieh and V. Shanov, *Small*, 2017, **13**, 1603114.

34 N. Lin, H. Chen, W. Wang and L. Lu, *Adv. Mater. Technol.*, 2021, **6**, 2000991.